Environmental Science & Technology

pubs.acs.org/est

Article

A Satellite-Based Indicator for Diagnosing Particulate Nitrate Sensitivity to Precursor Emissions: Application to East Asia, Europe, and North America

Ruijun Dang,* Daniel J. Jacob, Shixian Zhai, Laura Hyesung Yang, Drew C. Pendergrass, Pierre Coheur, Lieven Clarisse, Martin Van Damme, Jin-soo Choi, Jin-soo Park, Zirui Liu, Peifu Xie, and Hong Liao

Cite This: *Environ. Sci. Technol.* 2024, 58, 20101−20113

Read Online

ACCESS | Metrics & More | Article Recommendations | Supporting Information

ABSTRACT: Particulate nitrate is a major component of fine particulate matter ($PM_{2.5}$) and a key target for improving air quality. Its formation is varyingly sensitive to emissions of nitrogen oxides ($NO_x \equiv NO + NO_2$), ammonia (NH_3), and volatile organic compounds (VOCs). Diagnosing the dominant sensitivity is critical for effective pollution control. Here, we show that satellite observations of the NO_2 column and the NH_3/NO_2 column ratio can effectively diagnose the dominant sensitivity regimes in polluted regions of East Asia, Europe, and North America, in different seasons, though with reduced performance in the summer. We demarcate the different sensitivity regimes using the GEOS-Chem chemical transport model and apply the method to satellite observations from the OMI (NO_2) and IASI (NH_3) in 2017. We find that the dominant sensitivity regimes vary across regions and remain largely consistent across seasons. Sensitivity to NH_3 emissions dominates in the northern North China Plain (NCP), the Yangtze River Delta, South Korea, most of Europe, Los Angeles, and the eastern United States. Sensitivity to NO_x emissions dominates in central China, the Po Valley in Italy, the central United States, and the Central Valley in California. Sensitivity to VOCs emissions dominates only in the southern NCP in the winter. These results agree well with those of previous local studies. Our satellite-based indicator provides a simple tool for air quality managers to choose emission control strategies for decreasing $PM_{2.5}$ nitrate pollution.

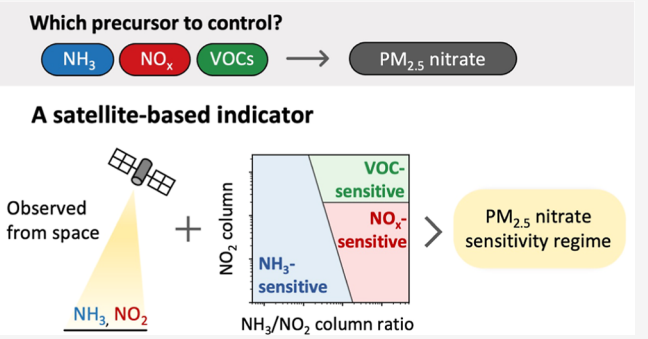

KEYWORDS: *$PM_{2.5}$ nitrate pollution, satellite indicator, sensitivity regime, air quality management, nitrogen oxides, ammonia, volatile organic compounds*

1. INTRODUCTION

Particulate nitrate is a major component of fine particulate matter ($PM_{2.5}$) and often drives $PM_{2.5}$ pollution events in the urbanized world.[1−5] It harms human health,[6] and its deposition can adversely impact the ecosystem, causing soil acidification,[7] eutrophication,[8] and biodiversity loss.[9] With sulfate and organic fractions of $PM_{2.5}$ decreasing in response to emission controls,[10,11] nitrate has emerged as a key target for further improving air quality.[12] In the eastern United States, wintertime nitrate concentrations exhibited no significant decrease between 2007 and 2015 despite a 36% reduction in NO_x emissions.[13] In eastern China, nitrate levels have remained unresponsive to NO_x emission controls over the past decade.[14−16] New emission control strategies may be needed to manage particulate nitrate to meet the $PM_{2.5}$ air quality targets.

Particulate nitrate is produced by the oxidation of nitrogen oxide radicals ($NO_x \equiv NO + NO_2$) to nitric acid (HNO_3), which condenses into the aerosol phase in the presence of alkalinity. We refer to pNO_3^- as the particulate nitrate in the fine mode ($PM_{2.5}$), and observations show that it originates mainly from co-condensation with ammonia (NH_3).[14,17,18] The pNO_3^-/HNO_3 thermodynamic equilibrium is highly sensitive to temperature and relative humidity, so that pNO_3^- concentrations are typically highest in winter−spring. The NO_x oxidation process involves the hydroxyl radical (OH) and ozone (O_3), both of which depend on the availability of NO_x and volatile organic compounds (VOCs). NO_x, NH_3, and VOCs are thus the three emitted gases serving as precursors for pNO_3^- formation. NO_x in polluted regions is mainly from fuel combustion.[19] NH_3 is from agriculture including fertilization

Received: August 4, 2024
Revised: September 20, 2024
Accepted: September 23, 2024
Published: October 28, 2024

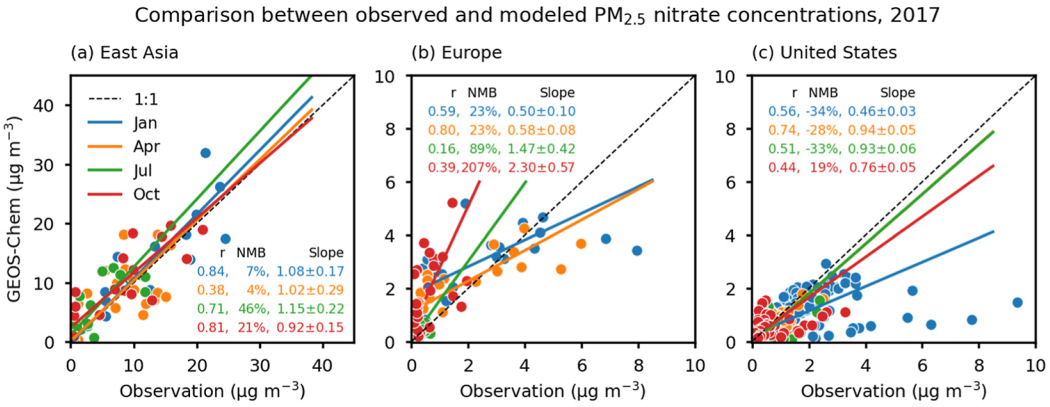

Figure 1. Comparison of observed and modeled monthly mean $PM_{2.5}$ nitrate concentrations at sites in (a) East Asia, (b) Europe, and (c) the United States for January, April, July, and October 2017. Comparison statistics include the correlation coefficient (r), normalized mean bias, and the reduced-major-axis (RMA) regression line and slope (±95% confidence interval). The 1:1 line is shown as a dashed line. The panels have different scales.

and manure[20] and also has sources from industry[21,22] and vehicles.[23] VOCs are from combustion, industrial and domestic chemical products, vegetation, and open fires.[24] Understanding which of these three emitted precursors is most important in driving pNO_3^- formation is critical to effective air quality management.

Formation of pNO_3^- is dominantly sensitive to either NH_3 or HNO_3 depending on which is in less supply.[25] This sensitivity can be determined using diagnostic indicators derived from aerosol and gas measurements[26,27] or with thermodynamic models using these measurements as input.[4,18] Although a dominant sensitivity to HNO_3 often suggests a corresponding sensitivity to NO_x emissions, the conversion of NO_x to HNO_3 can in fact be limited by VOCs availability under VOC-limited (NO_x-saturated) conditions for O_3 formation, a situation that frequently occurs in urban environments during winter.[16,28] Other factors further complicate the relationship between pNO_3^- and its precursors, including competing deposition of HNO_3 and pNO_3^-,[14,25] conversion of NO_x to organic nitrates,[29] uptake of HNO_3 by alkaline soil dust and sea salt,[30] and competition from sulfate for available NH_3.[31] Chemical transport models (CTMs) can provide a comprehensive description of these processes and serve as a useful tool for diagnosing pNO_3^- sensitivity to emissions through simulations with perturbed emissions.[14,16,32] However, this approach is computationally laborious and subject to model errors, in particular, for emissions.

Satellites measure tropospheric columns of NO_2 (Ω_{NO2}), formaldehyde (Ω_{HCHO}), and NH_3 (Ω_{NH3}). Space-based NO_2 and HCHO measurements started with the GOME instrument in 1995,[33] followed by OMI in 2005[34] and TROPOMI in 2017,[35] and are now expanding with the geostationary constellation including GEMS over East Asia in 2020,[36] TEMPO over North America in 2023,[37] and the Sentinel-4 satellite over Europe to be launched in 2025.[38] For NH_3, space-based measurements began with the TES instrument in 2004,[39] followed by IASI in 2007,[40] CrIS in 2012,[41] and soon-to-be-launched IRS on Sentinel-4.[42]

In previous work, we introduced a new satellite-based method using the $\Omega_{NH3}/\Omega_{NO2}$ ratio together with Ω_{NO2} to identify the dominant sensitivity of local fine pNO_3^- formation to emissions of NO_x, NH_3, and VOCs under wintertime conditions in East Asia.[43] The approach is similar to the use of the $\Omega_{HCHO}/\Omega_{NO2}$ ratio for diagnosing NO_x- versus VOC-limited conditions for summertime ozone formation.[44−46] Although Ω_{HCHO} is a useful diagnostic of VOCs reactivity in summer, we found that Ω_{NO2} was a more useful indicator of VOC-limited conditions for pNO_3^- formation because of the low Ω_{HCHO} detection capability in winter.[47]

Here, we use GEOS-Chem CTM to demonstrate the generalization of our satellite-based indicator to other seasons and to Europe and North America. We then apply this method to satellite observations of OMI NO_2 and IASI NH_3 to identify the seasonality and regionality of pNO_3^- sensitivity regimes. We evaluate our satellite-determined regimes with previous local studies and discuss their implications for air quality management.

2. MATERIALS AND METHODS

2.1. GEOS-Chem Model. We use the GEOS-Chem CTM (version 13.4.1, DOI: https://zenodo.org/record/6564702) to examine how pNO_3^- formation sensitivity to emissions can be diagnosed from the satellite column observations. The simulations are driven by MERRA-2 meteorology and are conducted at a nested resolution of 0.5° × 0.625° (≈50 × 50 km^2) over East Asia (90° to 145°E, 10° to 55°N), Europe (20°W to 40°E, 30° to 65°N), and North America (135° to 55°W, 15° to 60°N), with boundary conditions updated every 3 h from a 4° × 5° global simulation. We conduct simulations for January, April, July, and October of 2017, and these are viewed in the text as representative of their respective seasons. The 4° × 5° global simulation is spun up for 6 months starting in July 2016 and provides the initial as well as the boundary conditions for the 0.5° × 0.625° continental simulations.

GEOS-Chem includes detailed oxidant−aerosol chemistry.[48] pNO_3^- formation in GEOS-Chem is mainly from the thermodynamic equilibrium within the H_2SO_4−HNO_3−HCl−NH_3 system, as described by the ISORROPIA II model.[49] Some of the pNO_3^- formation can take place by aerosol uptake and hydrolysis of organic nitrates.[50] GEOS-Chem also includes nitrate formation from uptake by alkaline sea salt[51] and soil dust,[52] but these components are mainly in the coarse size range and generally make little contribution to $PM_{2.5}$. Simulation of pNO_3^- is challenging for CTMs because of the complexity and nonlinearity of the processes involved,[53,54] but recent versions of GEOS-Chem show little bias and the ability to capture pNO_3^- variability.[14,43,55,56]

https://doi.org/10.1021/acs.est.4c08082
Environ. Sci. Technol. 2024, 58, 20101−20113

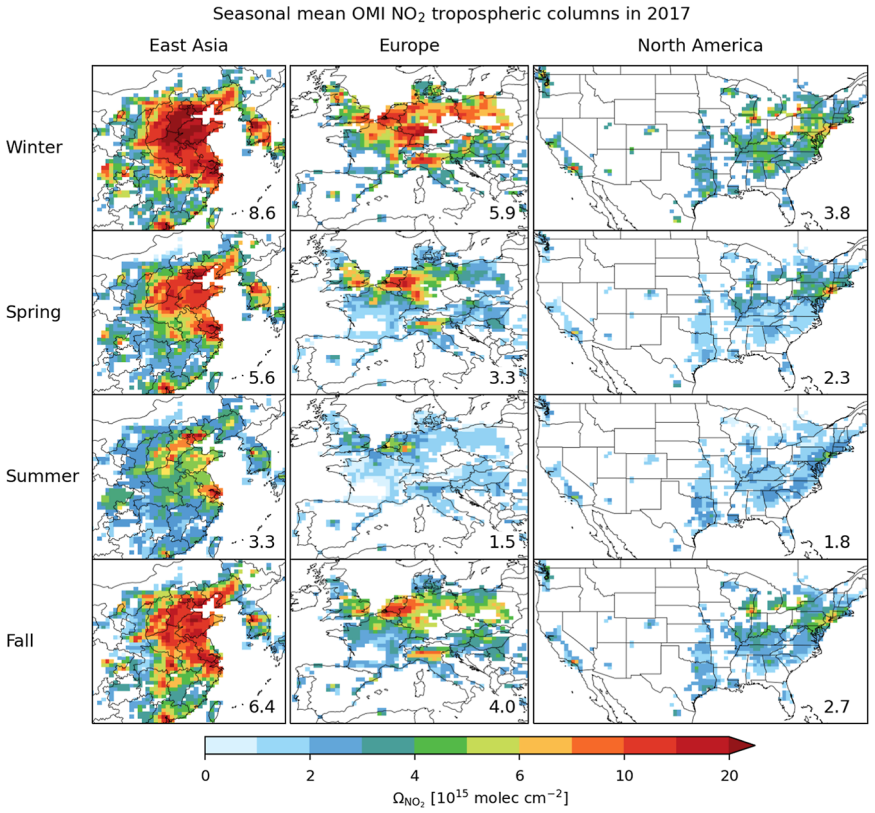

Figure 2. Seasonal mean OMI tropospheric NO_2 columns (Ω_{NO2}) in polluted regions of East Asia, Europe, and North America in 2017. Values are plotted on the 0.5° × 0.625° GEOS-Chem model grid as 3 month averages for winter (DJF), spring (MAM), summer (JJA), and fall (SON). Cleaner grid cells with winter $\Omega_{NO2} < 2.5 \times 10^{15}$ molecules cm^{-2} are excluded. Regional mean values are provided (inset), with units of 10^{15} molecules cm^{-2}.

Our simulation is the same as previously described in Dang et al.,[43] featuring specific options within the standard GEOS-Chem v.13.4.1. These include the use of Luo's wet deposition scheme to better reproduce pNO_3^- concentrations[55,56] and the incorporation of aerosol nitrate photolysis, which improves the simulation of tropospheric NO_2 columns.[57] Anthropogenic emissions are from the global Community Emissions Data System (CEDSv2) inventory[58] superseded by region-specific inventories including MEIC for China,[59] KORUSv5 for South Korea,[60] and US EPA NEI 2016 for the United States (https://www.epa.gov/air-emissions-modeling/2016v1-platform). Biomass burning emissions are from the Global Fire Emissions Database version 4 with small fires (GFED4s).[61] Soil NO_x emissions are calculated following Hudman et al.[62] with updates from Wang et al.[63] Lightning NO_x emissions are computed based on Murray et al.[64] Biogenic VOCs emissions are described by MEGAN v2.1.[65]

Our use of GEOS-Chem for the interpretation of satellite observations in terms of the pNO_3^- sensitivity regime relies on the model having a correct representation of pNO_3^- formation processes but not necessarily emissions. Here, we evaluate the model's performance in simulating pNO_3^- by comparison to $PM_{2.5}$ surface measurements in 2017 from East Asia, Europe, and the United States. East Asian data are collected from previous studies in China[14,66−75] and from sites managed by South Korea's National Institute of Environmental Research and the Acid Deposition Monitoring Network in East Asia (EANET), totaling 22 sites. Site details and pNO_3^- data are provided at 10.7910/DVN/CQO0E8. European data are from the European Monitoring and Evaluation Programme network (EMEP, 24 sites) (https://ebas-data.nilu.no/Default.aspx). US data are from the Interagency Monitoring of Protected Visual Environments network (IMPROVE, 147 sites) and the Chemical Speciation Network (CSN, 132 sites) (http://views.cira.colostate.edu/fed/QueryWizard/Default.aspx).

Figure 1 compares observed versus modeled monthly mean surface pNO_3^- concentrations for January, April, July, and October 2017. Observations within the same grid cell are averaged and then compared to the model results. GEOS-Chem simulates pNO_3^- in East Asia remarkably well across the four seasons. Results in Europe and the United States show relatively larger errors, which may reflect lower concentrations and dynamic range. Some of the EMEP sites are remote, and the model overestimates pNO_3^- there. The model tends to underestimate the high observed pNO_3^- concentrations at sites in the western urban United States during winter probably due to a low bias in winter NH_3 emissions.[76]

Here, we diagnose the sensitivities of pNO_3^- formation to NO_x, NH_3, and VOCs emissions in the model world with the purpose of applying the resulting concentration-based diagnostics to the real world where emissions may be different from the model. The idea is that the model can properly relate the sensitivities to observable satellite column concentrations even if the model emissions are incorrect. The exact same approach is used when constructing $HCHO/NO_2$ column diagnostics of the ozone production regime.[45] We conduct GEOS-Chem sensitivity simulations with 20% reduction of individual precursor emissions. The local model sensitivity (S_i) of pNO_3^- to the emissions (E_i) of precursor i is calculated

https://doi.org/10.1021/acs.est.4c08082
Environ. Sci. Technol. 2024, 58, 20101−20113

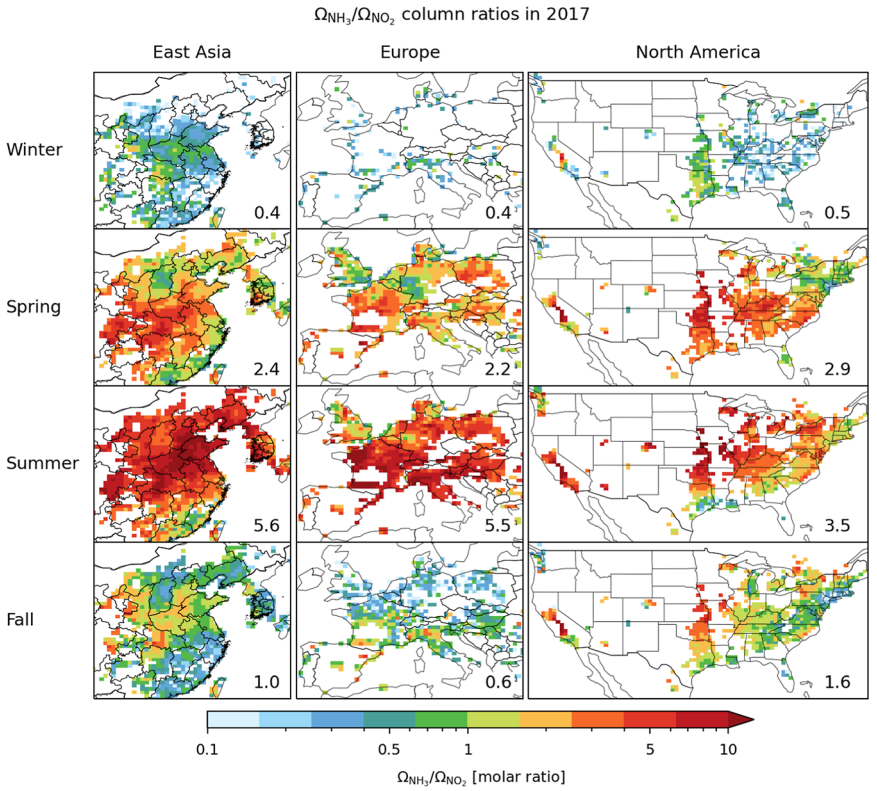

Figure 3. Same as Figure 2 but showing column ratios $\Omega_{NH3}/\Omega_{NO2}$. The seasonal mean column ratios are computed as the ratios of the means. Regional mean ratios are inset.

from the relative model differences (Δ) between the sensitivity and base simulations as

$$S_i = \frac{\Delta \log [pNO_3^-]}{\Delta \log E_i} \quad (1)$$

where $[pNO_3^-]$ refers to monthly mean concentrations in surface air, and i refers to NH_3, NO_x, or VOCs. A higher S_i value indicates greater sensitivity. By comparing the sensitivities S_{NOx}, S_{NH3}, and S_{VOC}, we can determine whether pNO_3^- formation in a model grid cell is most NO_x-, NH_3-, or VOC-sensitive.

2.2. Satellite Observations of NO_2 and NH_3. We used satellite observations of NO_2 columns and NH_3/NO_2 column ratios to identify which precursor emissions are most responsible for pNO_3^- formation. Here, the same satellite products are used as in our previous work:[43] version 4 of the NASA OMI NO_2 level 2 product (https://disc.gsfc.nasa.gov/datasets/OMNO2_003/summary) and version 3 of the reanalyzed level 2 IASI NH_3 product (https://iasi.aeris-data.fr/catalog/#masthead).

The OMI retrieval measures NO_2 slant columns by fitting the backscattered solar spectrum and converts the data to tropospheric vertical columns.[34] It provides daily coverage at 13:30 local time (LT) with a spatial resolution of 13 × 24 km^2 at the nadir. We filter out pixels with cloud fraction >0.3, surface reflectance >0.3, solar zenith angle >75°, and viewing zenith angle >65° and those affected by the so-called row anomaly. The IASI instrument measures atmospheric NH_3 columns using thermal infrared radiation emitted by the Earth's surface and atmosphere.[77] It offers global coverage twice daily, at 9:30 and 21:30 LT, with a nadir pixel resolution of 12 × 12 km^2. We use only 9:30 LT observations to minimize the time separation with OMI and only clear-sky scenes with cloud fraction <0.1.[78] Different cloud fraction thresholds are used for NO_2 and NH_3 as they use different cloud retrievals. Both pixel observations of NO_2 and NH_3 are gridded and averaged to a resolution of 0.5° × 0.625° to calculate seasonal mean columns. Only grid cells with more than 30 successful retrievals are included in the analysis. Further filtering is applied to the gridded seasonal means to remove negative values.

Figure 2 shows the seasonal mean NO_2 columns (Ω_{NO2}) measured by the OMI in 2017. We focus on polluted areas defined by their winter $\Omega_{NO2} > 2.5 \times 10^{15}$ molecules cm^{-2}, excluding cleaner areas where diagnosing sensitivity to local emissions would be inappropriate. OMI observes high NO_2 in densely populated regions. Ω_{NO2} peaks in winter and is lowest during summer, reflecting the seasonality in photochemical oxidation. High NH_3 columns concentrations (Ω_{NH3}) are observed in agriculturally intensive areas[79] (Figure S1). Peak Ω_{NH3} levels occur in summer, followed by spring, driven by fertilizer application and high temperatures.[80] The different seasonalities of Ω_{NO2} and Ω_{NH3} imprint a large seasonality to the $\Omega_{NH3}/\Omega_{NO2}$ ratio (Figure 3). The ratio peaks in the summer, with seasonal mean values exceeding 10, and drops to below unity in the winter.

3. RESULTS AND DISCUSSION

3.1. Particulate Nitrate Sensitivity Regimes in GEOS-Chem. Previous work by Dang et al.[43] for wintertime conditions in East Asia found that the modeled dominant sensitivities (NO_x-, NH_3-, or VOC-sensitive) could be separated within a two-dimensional space defined by the column concentration indicator $\Omega_{NH3}/\Omega_{NO2}$ and Ω_{NO2}. The

https://doi.org/10.1021/acs.est.4c08082
Environ. Sci. Technol. 2024, 58, 20101−20113

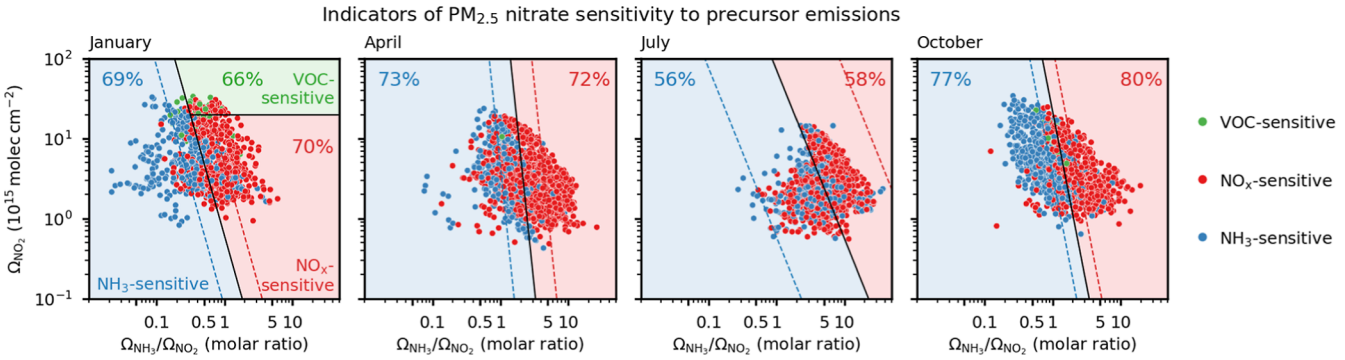

Figure 4. Performance of satellite-based indicator for diagnosing $PM_{2.5}$ nitrate (pNO_3^-) formation sensitivity in the GEOS-Chem model in different seasons. Circles indicate the dominant monthly mean sensitivities of surface pNO_3^- formation (either NH_3-, NO_x-, or VOC-sensitive) in polluted 0.5° × 0.625° model grid cells across East Asia, Europe, and North America (shown in Figure 2). These dominant sensitivities are plotted in an indicator state space as observable from satellite measurements: the $\Omega_{NH3}/\Omega_{NO2}$ column ratio and the Ω_{NO2} column. Ω_{NH3} and Ω_{NO2} columns are sampled to mimic the overpass times of IASI and OMI instruments, respectively. LDA establishes thresholds (black solid lines) to separate different regimes, with additional delineations (blue/red dashed lines) indicating higher confidence levels (>80%) for NH_3- and NO_x-sensitive regimes. Equations 2a−2c with coefficients in Table 1 defines the threshold lines. Inset numbers indicate the accuracy in classifying the model dominant sensitivities using black solid thresholds.

$\Omega_{NH3}/\Omega_{NO2}$ ratio indicates the relative abundance of NH_3 to NO_x, while a high Ω_{NO2} level diagnoses VOC-limited conditions in the oxidation of NO_x to HNO_3. Figure 4 expands this analysis to other seasons and regions, where the circles represent the dominant sensitivities of pNO_3^- formation for individual 0.5° × 0.625° grid cells in polluted regions (as defined in Figure 2). The column indicator is sampled in GEOS-Chem at the OMI overpass time of 13−14 LT for NO_2 and at the IASI overpass time of 9−10 LT for NH_3 to emulate satellite observations. Averaging kernels are applied to the model NO_2 vertical profiles following Cooper et al.[81] to emulate tropospheric NO_2 columns from version 4 of the NASA OMI NO_2 level 2 product (OMNO2).[34] Modeled NH_3 columns are directly used to emulate version 3 of the IASI NH_3 product as averaging kernels are not provided by that product.[82]

Figure 4 shows that application of the satellite-based indicator to diagnose dominant pNO_3^- sensitivities to precursor emissions can be generalized to other regions and seasons with reduced performance in summer. We find similarity of behavior in relating pNO_3^- sensitivity to the satellite-based indicator for individual regions, and therefore all three regions are grouped in Figure 4. Linear discriminant analysis (LDA) in the ($\log \Omega_{NH3}/\Omega_{NO2}$, $\log \Omega_{NO2}$) space is used to delineate transitions between regimes. LDA is a classifier algorithm that finds the linear boundary that maximizes the separation between classes and provides estimated probabilities of belonging to a specific class. This approach is suitable for our case as Figure S2 shows clear linear boundaries between regimes when using logarithms of surface concentrations ($\log [NH_3]/[NO_2]$ and $\log [NO_2]$) as indicators. These linear boundaries are less distinct in Figure 4 with satellite indicators due to the complex column−surface relationship. Black solid lines indicate delineation with 50% probability, and dashed lines indicate delineation with probabilities >80%.

As found under winter conditions in East Asia,[43] NH_3-sensitive conditions are associated with $\Omega_{NH3}/\Omega_{NO2}$ ratios below a certain threshold, which decreases with increasing Ω_{NO2}. This dependence of the $\Omega_{NH3}/\Omega_{NO2}$ threshold on Ω_{NO2} is due to the reduced efficiency of NO_2 conversion to HNO_3 as the NO_x increases, leading to a more likely NH_3 excess at a given $\Omega_{NH3}/\Omega_{NO2}$ ratio. Outside of the NH_3-sensitive regime, whether NO_x or VOCs is the controlling precursor is well delineated by Ω_{NO2} levels. $\Omega_{NO2} > 2 \times 10^{16}$ molecules cm^{-2} indicates a strong VOC-limited condition for oxidant formation, making pNO_3^- dominantly sensitive to VOCs emissions (mainly found in winter conditions). For $\Omega_{NO2} < 2 \times 10^{16}$ molecules cm^{-2}, the sensitivity is mostly to NO_x emissions.

The ($\Omega_{NH3}/\Omega_{NO2}$, Ω_{NO2}) thresholds shown as black solid lines in Figure 4 diagnose the dominant sensitivity for pNO_3^- formation in GEOS-Chem with an accuracy of 70−80% (misclassification rate of 20−30%) except in summer. The lower accuracy in summer (~60%) is mainly due to (1) the coexistence of NH_3 and HNO_3 in the gas phase at warmer temperatures, reducing the contrast between sensitivities to NH_3 and NO_2, and (2) increased contributions from the free troposphere to NO_2 column concentrations, making satellite observations less representative of surface conditions.[83,84] Other factors may also affect the accuracy, such as the representation error caused by using morning/afternoon satellite measurements to represent daily averages. The accuracy rises above 90% for the thresholds defined by dashed lines, indicating high-confidence zones.

The threshold for separating the NH_3- and NO_x-sensitive regimes exhibits seasonal variability, shifting rightward along the $\Omega_{NH3}/\Omega_{NO2}$ axis in warmer seasons. This shift is driven by seasonal variations in the column-to-surface relationship. In warmer seasons, the columns become less representative of surface conditions for both NH_3 and NO_2 due to the increased uplift of surface pollution to the free troposphere and a greater influence of background lightning contributions on the NO_2 columns. The sensitivity regimes, delineated by the solid and dashed lines in Figure 4, are thus diagnosed from $\Omega_{NH3}/\Omega_{NO2}$ and Ω_{NO2} as

$$NH_3\text{-sensitive: } \log \frac{\Omega_{NH_3}}{\Omega_{NO_2}} < b + k \log \Omega_{NO_2} \quad (2a)$$

https://doi.org/10.1021/acs.est.4c08082
Environ. Sci. Technol. 2024, 58, 20101−20113

$$\text{NO}_x\text{-sensitive: } \log\frac{\Omega_{\text{NH}_3}}{\Omega_{\text{NO}_2}} > b + k\log\Omega_{\text{NO}_2} \quad \text{and } \Omega_{\text{NO}_2} < y_0 \tag{2b}$$

$$\text{VOC-sensitive: } \log\frac{\Omega_{\text{NH}_3}}{\Omega_{\text{NO}_2}} > b + k\log\Omega_{\text{NO}_2} \quad \text{and } \Omega_{\text{NO}_2} > y_0 \tag{2c}$$

where the coefficients b, k, and y_0 for different seasons are given in Table 1. Entries b_1 and b_2 define the high-confidence

Table 1. Threshold Coefficients for Separating pNO_3^- Sensitivity Regimes in Equations 2a–2c[a]

	winter (DJF)	spring (MAM)	summer (JJA)	fall (SON)
k	−0.33	−0.13	−0.47	−0.23
b[b]	−0.070	0.40	0.88	0.31
b_1[b]	−0.36	0.08	−0.10	0.12
b_2[b]	0.22	0.71	1.87	0.49
y_0[c]	20	>20	>20	>20

[a]With $\Omega_{NH3}/\Omega_{NO2}$ in units of molar ratio and Ω_{NO2} in units of 10^{15} molecules cm^{-2}. [b]For thresholding between dominant NH_3- and NO_x-sensitive regimes (b, solid lines in Figure 4), high confidence (>80%) for a dominant NH_3-sensitive regime (b_1, dashed lines in Figure 4) and high confidence (>80%) for a NO_x-sensitive regime (b_2, dashed lines in Figure 4). [c]No dominant VOC-sensitive conditions were found in the GEOS-Chem simulation for seasons other than winter.

(>80%) thresholds for the NH_3-sensitive and NO_x-sensitive regimes, respectively (dashed lines in Figure 4), VOC-sensitive conditions are limited to winter with $\Omega_{NO2} > 2 \times 10^{16}$ molecules cm^{-2}.

3.2. Application to Satellite Observations. We now diagnose local pNO_3^- sensitivity regimes across East Asia, Europe, and North America for different seasons in 2017 by applying the model thresholds from eqs 2a–2c to the OMI and IASI satellite observations of ($\Omega_{NH3}/\Omega_{NO2}$, Ω_{NO2}), as shown in Figures 2 and 3. Figure 5 shows the spatial distribution of the dominant sensitivities to emissions inferred from the satellite indicator. Dark blue/red colors indicate regions diagnosed with >80% confidence levels. Winter data in Europe are sparse due to low number of successful NH_3 retrievals.[85]

The satellite measurements indicate varying pNO_3^- sensitivity regimes across regions. Focusing on winter, when pNO_3^- pollution is most severe (first row of Figure 5), NH_3-sensitive regimes are identified in areas with relatively low $\Omega_{NH3}/\Omega_{NO2}$ ratios. These include the northern North China Plain (NCP, including Beijing), the Yangtze River Delta (YRD, including Shanghai), the Seoul Metropolitan Area, most of Europe, Los Angeles, and eastern United States. In these regions, reducing NH_3 emissions is the most effective method to reduce winter pNO_3^- concentrations. NO_x-sensitive regimes are identified in areas with higher $\Omega_{NH3}/\Omega_{NO2}$ ratios and relatively low Ω_{NO2} including central China (Fen-Wei Plain, Sichuan Basin, and Hubei and Hunan provinces), the Po Valley in Italy, the central United States, and the Central Valley in California. These are agricultural areas with high NH_3 emissions even in winter, so reducing NO_x emissions is most effective for controlling winter pNO_3^- levels. Dominant VOC-sensitive conditions are found in the southern NCP, characterized by both NH_3 saturation ($\Omega_{NH3}/\Omega_{NO2}$ ratio >0.4, Figure 3) and very high Ω_{NO2} (>2×10^{16} molecules cm^{-2}, Figure 2). In this region, the most effective approach to decrease winter pNO_3^- is to control VOCs emissions.

Both $\Omega_{NH3}/\Omega_{NO2}$ and Ω_{NO2} exhibit significant seasonal variations, as discussed in Section 2.2. The $\Omega_{NH3}/\Omega_{NO2}$ ratio is lowest in the winter and highest in the summer, while Ω_{NO2} shows the opposite pattern. Despite these variations, the spatial pattern of dominant sensitivities, specifically the NO_x- and NH_3-sensitive regions, remains largely consistent throughout the year. This is because of the shift in the demarcation between regimes in Figure 4. Ω_{NO2} may be low in summer, but the HNO_3 production rate is larger than in winter. The VOC-sensitive regime is limited to winter, as would be expected, because VOCs limitation of oxidant chemistry is weaker in other seasons.

3.3. Comparisons to Local Studies. Tables 2–4 compare the pNO_3^- sensitivities identified from the satellite indicator with results from local studies in East Asia, Europe, and the United States. We collect three kinds of local studies from the literature: (1) field studies that measure gas and aerosol concentrations and use observational indicators or thermodynamic models to identify the dominant sensitivities; (2) COVID studies that examine the response of pNO_3^- levels to real-world NO_x reductions during the COVID-19 pandemic; and (3) regional CTM studies that quantify the response of pNO_3^- levels to perturbed precursor emissions of NO_x, NH_3, or VOCs. Most of the studies focused on only one season. The field studies diagnose NH_3 and HNO_3 sensitivities, and some relate HNO_3 sensitivities to NO_x and VOCs emissions using an oxidant chemistry model. HNO_3 sensitivity generally implies sensitivity to NO_x emissions, except under urban winter conditions where it implies sensitivity to VOCs emissions.[28] The COVID studies diagnose whether or not pNO_3^- is sensitive to NO_x emission reductions.[75,86,87]

Our results align in general very well with these local studies, which find pNO_3^- formation to be NH_3-sensitive in Guangzhou (fall),[88] Germany (spring),[87] the Northeast United States (winter), the Southeast United States (summer), and Los Angeles (summer)[18] and to be HNO_3-sensitive in Jinan, NCP (summer),[89] central China (all seasons),[86,90] the Po Valley (all seasons),[91] Paris (spring),[92] and the Central Valley in California (winter).[93−95] Our satellite-based indicator can successfully distinguish spatial contrasts between NH_3-sensitive and NO_x-sensitive regions, and the consistency in regimes across seasons also agrees well with previous local studies. Using the WRF-Chem model, Li et al.[32] found an increased sensitivity to NO_x during summer in the NCP and YRD, due to a shift to the transitional/NO_x-sensitive regime for oxidant formation. We also find a larger area of NO_x-sensitive conditions in eastern China in the summer. Summertime pNO_3^- is important in China where it can contribute to pollution episodes.[96,97]

Some urban field studies in winter including in Beijing, Nanjing, Shanghai, and Salt Lake City concluded that pNO_3^- formation is more sensitive to HNO_3 than NH_3 due to an observed excess of NH_3.[4,18,75,99] However, we find these environments to be dominantly NH_3-sensitive. This may be explained by differences in the lifetimes of HNO_3 and pNO_3^- against deposition that drive greater sensitivity to NH_3 even when NH_3 concentrations are in excess.[14,25,43] CTM studies for urban winter conditions, which would include the deposition effect, report results consistent with ours, including

https://doi.org/10.1021/acs.est.4c08082
Environ. Sci. Technol. 2024, 58, 20101−20113

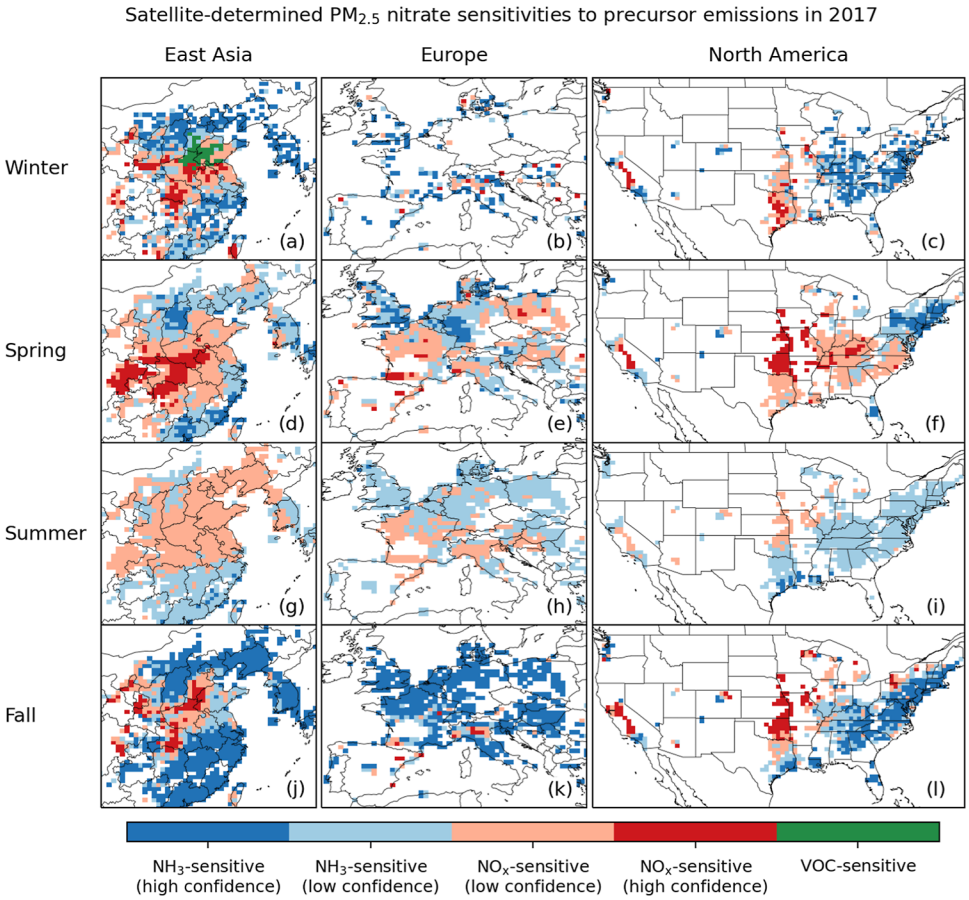

Figure 5. Dominant sensitivities of $PM_{2.5}$ nitrate (pNO_3^-) to precursor emissions in polluted regions of East Asia, Europe, and North America in 2017, as diagnosed from seasonal mean IASI and OMI satellite observations of tropospheric NH_3 and NO_2 columns. The regimes are diagnosed using the threshold lines from Figure 4 (eqs 2a–2c with coefficients from Table 1). White areas indicate either lack of data or cleaner areas (winter $\Omega_{NO2} < 2.5 \times 10^{15}$ molecules cm^{-2}).

Table 2. $PM_{2.5}$ Nitrate Sensitivity in East Asia: Comparison to Previous Studies

previous study	season	study type	finding	this work
North China Plain				
Regional[14,16,32]	winter	CTM	NH_3- and VOC-sensitive	NH_3- and VOC-sensitive
Regional[32]	summer	CTM	NO_x- and NH_3-sensitive	NO_x-sensitive
Beijing[18,86]	winter	field	HNO_3-sensitive	NH_3-sensitive
		COVID	but NO_x-insensitive	
Jinan[89]	summer	field	HNO_3-sensitive	NO_x-sensitive
Yangtze River Delta				
Regional[32,98]	winter	CTM	NH_3-sensitive	NH_3-sensitive
Regional[32]	summer	CTM	NH_3-sensitive	NH_3- and NO_x-sensitive
Nanjing[86,99]	winter	field	HNO_3-sensitive	NH_3-sensitive
		COVID	but NO_x-insensitive	
Shanghai[75]	winter	field	HNO_3-sensitive	NH_3-sensitive
		COVID	but NO_x-insensitive	
Central China				
Changsha[86]	winter	COVID	NO_x-sensitive	NO_x-sensitive
Wuhan[90]	all seasons	field	HNO_3-sensitive	NO_x-sensitive
South China				
Guangzhou[88]	fall	field	NH_3-sensitive	NH_3-sensitive

dominant sensitivities to NH_3 and VOCs emissions in the NCP[14,16,32] and to NH_3 in the YRD.[32]

Our results showing NH_3- and VOC-sensitive regimes in winter NCP and NH_3-sensitive regimes in the Northeast United States also align with long-term observations that winter pNO_3^- concentrations in these regions have remained flat in recent years, showing insensitivity to NO_x reductions.[13−16] One discrepancy that we cannot explain is for Cabauw (Netherlands), where a field study indicates a HNO_3-

https://doi.org/10.1021/acs.est.4c08082
Environ. Sci. Technol. 2024, 58, 20101−20113

Table 3. Same as Table 2 but for Europe

previous study	season	study type	finding	this work
Cabauw, Netherlands[18]	all seasons	field	HNO_3-sensitive	NH_3-sensitive
Po Valley, Italy[91]	all seasons	field	HNO_3-sensitive	NO_x-sensitive
Paris, France[92]	spring	COVID	NO_x-sensitive	NO_x-sensitive
Germany[87]	spring	COVID	NO_x-insensitive	NH_3-sensitive

Table 4. Same as Table 2 but for the United States (US)

previous study	season	study type	finding	this work
Northeast United States				
Regional[18]	winter	field	NH_3-sensitive	NH_3-sensitive
Western United States				
Salt Lake City[4,28]	winter	field	HNO_3-sensitive, VOC-sensitive	NH_3-sensitive
Central Valley[93−95]	winter	field	HNO_3-sensitive	NO_x-sensitive
Los Angeles[18]	summer	field	NH_3-sensitive	NH_3-sensitive
Southeast United States				
Regional[18]	summer	field	NH_3-sensitive	NH_3-sensitive

sensitive regime in all seasons,[18] while our satellite indicator finds a NH_3-sensitive regime.

3.4. Application to Air Quality Management. Following our work, air quality managers can use satellite observations of $\Omega_{NH3}/\Omega_{NO2}$ and Ω_{NO2} based on Figure 4 to diagnose whether pNO_3^- in their region is dominantly NH_3-, NO_x-, or VOC-sensitive. This is very much like the well-established use of the $HCHO/NO_2$ ratio to diagnose whether ozone production is either NO_x-limited or VOC-limited. Air quality managers can further track the evolution of the sensitivity over time by monitoring the changes in $\Omega_{NH3}/\Omega_{NO2}$ and Ω_{NO2} in successive years. For example, plotting data from successive years in Figure 4, as NO_x emissions decrease and as NH_3 increases (because SO_2 emissions decrease), could document an evolution toward NO_x-sensitive conditions. Compared with traditional approaches based on models or field measurements, this satellite-based method provides more comprehensive spatial coverage, enables long-term monitoring, requires less computational effort, and is not subject to emission input errors that affect models.

There are, however, several precautions to keep in mind. The diagnostic should be done on the scale of polluted source regions (we used 50 km here and required $\Omega_{NO2} > 2.5 \times 10^{15}$ molecules cm^{-2}) rather than finer scales or regions far downwind of emissions. The reason is that the relationship among pNO_3^-, Ω_{NH3}, and Ω_{NO2} reflects the mechanistic dependence of pNO_3^- formation on NH_3 and NO_x emissions within the region. A patchwork of NH_3-sensitive and NO_x-sensitive grid cells on a 50 km scale would require cautious interpretation. We see from Figure 5 that the diagnostic is consistent across broad regions, which supports its reliability.

The diagnosis should be done using seasonal or monthly mean values for the satellite columns with the filtering described in this paper. Shorter periods are subject to noise. In that regard, the diagnosis is more relevant to seasonal or annual mean $PM_{2.5}$ rather than to pollution events. Wintertime observations of NH_3 may not be available at high northern latitudes (Figure S1). The blank regions in Figure 5 indicates where/when the method is not applicable.

The thresholds for defining sensitivity regimes are derived from the GEOS-Chem model, and biases in that model could propagate in biases in the identification of sensitivity regimes. The ability of the model to reproduce observed pNO_3^- variability (Figure 1) and the verification against local studies (Tables 2−4) support the general use of the thresholds defined here. But verification with a different model or with a field study could be useful to support application for specific regions.

We used IASI and OMI in this work, but any current satellite observations could be used (CrIS for NH_3; TROPOMI, GEMS, and TEMPO for NO_2) as long as they are unbiased. This has been verified for the TROPOMI[100] and GEMS[101] NO_2 observations. There is unresolved bias for CrIS NH_3 retrievals[102,103] that would require further evaluation and correction. New satellite missions may improve the application of our satellite diagnostics by providing a higher density of observations and by measuring NH_3 and NO_2 from the same platform. This is expected from the geostationary satellites Sentinel-4[38] over Europe and GeoXO over North America,[104] as well as from the proposed Nitrosat mission.[105]

In summary, we have shown that a new satellite-based indicator using measurements of NO_2 and NH_3 columns can diagnose the sensitivity of $PM_{2.5}$ nitrate formation to NO_x, NH_3, and VOCs emissions in polluted regions of East Asia, Europe, and North America across all seasons, although with reduced performance in summer. We demonstrated the effectiveness of the indicator in the GEOS-Chem model and derived thresholds to demarcate the dominant sensitivity regimes in different seasons. By applying this method to OMI NO_2 and IASI NH_3 observations, we found that some regions are dominantly NO_x-sensitive, while others are dominantly NH_3-sensitive, consistently across seasons. VOC-sensitive conditions are limited to urban areas in winter with high NH_3 and very high NO_2. We compared our satellite-determined regimes with those of previous local studies and found good consistency. Our results emphasize the need for tailored emission control strategies to mitigate $PM_{2.5}$ nitrate pollution.

■ ASSOCIATED CONTENT

Supporting Information

The Supporting Information is available free of charge at https://pubs.acs.org/doi/10.1021/acs.est.4c08082.

Additional materials about the IASI NH_3 observations; and the performance of surface indicator in the GEOS-Chem model (PDF)

https://doi.org/10.1021/acs.est.4c08082
Environ. Sci. Technol. 2024, 58, 20101−20113

AUTHOR INFORMATION

Corresponding Author

Ruijun Dang − *John A. Paulson School of Engineering and Applied Sciences, Harvard University, Cambridge, Massachusetts 02138, United States;* orcid.org/0000-0002-7662-3816; Email: rjdang@g.harvard.edu

Authors

Daniel J. Jacob − *John A. Paulson School of Engineering and Applied Sciences, Harvard University, Cambridge, Massachusetts 02138, United States*

Shixian Zhai − *Department of Earth and Environmental Sciences, Faculty of Science, The Chinese University of Hong Kong, Hong Kong, China;* orcid.org/0000-0002-0073-7809

Laura Hyesung Yang − *John A. Paulson School of Engineering and Applied Sciences, Harvard University, Cambridge, Massachusetts 02138, United States*

Drew C. Pendergrass − *John A. Paulson School of Engineering and Applied Sciences, Harvard University, Cambridge, Massachusetts 02138, United States*

Pierre Coheur − *Université Libre de Bruxelles (ULB), Spectroscopy, Quantum Chemistry and Atmospheric Remote Sensing (SQUARES), Brussels 1050, Belgium*

Lieven Clarisse − *Université Libre de Bruxelles (ULB), Spectroscopy, Quantum Chemistry and Atmospheric Remote Sensing (SQUARES), Brussels 1050, Belgium*

Martin Van Damme − *Université Libre de Bruxelles (ULB), Spectroscopy, Quantum Chemistry and Atmospheric Remote Sensing (SQUARES), Brussels 1050, Belgium; Royal Belgian Institute for Space Aeronomy (BIRA-IASB), Brussels 1180, Belgium*

Jin-soo Choi − *Air Quality Research Division, National Institute of Environmental Research, Incheon 22689, South Korea*

Jin-soo Park − *Air Quality Research Division, National Institute of Environmental Research, Incheon 22689, South Korea*

Zirui Liu − *State Key Laboratory of Atmospheric Environment and Extreme Meteorology, Institute of Atmospheric Physics, Chinese Academy of Sciences, Beijing 100029, China;* orcid.org/0000-0002-1939-9715

Peifu Xie − *Jiangsu Key Laboratory of Atmospheric Environment Monitoring and Pollution Control, Collaborative Innovation Center of Atmospheric Environment and Equipment Technology, School of Environmental Science and Engineering, Nanjing University of Information Science and Technology, Nanjing 210044, China*

Hong Liao − *Jiangsu Key Laboratory of Atmospheric Environment Monitoring and Pollution Control, Collaborative Innovation Center of Atmospheric Environment and Equipment Technology, School of Environmental Science and Engineering, Nanjing University of Information Science and Technology, Nanjing 210044, China;* orcid.org/0000-0001-6628-1798

Complete contact information is available at: https://pubs.acs.org/10.1021/acs.est.4c08082

Author Contributions

R.D. and D.J.J. designed the study. R.D. conducted model simulations and data analysis, with contributions from D.J.J., S.Z., L.H.Y., and D.C.P. P.C., L.C., and M.V.D. provided guidance on the analysis of the NH_3 satellite product. D.C.P., J.C., J.P., Z.L., H.L., and P.X. contributed to the measurement/collection of $PM_{2.5}$ composition data. R.D. led the writing with contributions from all authors.

Notes

The authors declare no competing financial interest.

ACKNOWLEDGMENTS

This work was supported by the Harvard−NUIST Joint Laboratory for Air Quality and Climate. The research in Belgium was supported by the Belgian Science Policy Office (BELSPO, Prodex HIRS and FED-tWIN ARENBERG projects) and the Air Liquide Foundation (TAPIR project). L.C. is a research associate supported by the Belgian F.R.S.-FNRS.

REFERENCES

(1) Tian, M.; Liu, Y.; Yang, F.; Zhang, L.; Peng, C.; Chen, Y.; Shi, G.; Wang, H.; Luo, B.; Jiang, C.; Li, B.; Takeda, N.; Koizumi, K. Increasing importance of nitrate formation for heavy aerosol pollution in two megacities in Sichuan Basin, southwest China. *Environ. Pollut.* **2019**, *250*, 898−905.

(2) Li, H.; Zhang, Q.; Zheng, B.; Chen, C.; Wu, N.; Guo, H.; Zhang, Y.; Zheng, Y.; Li, X.; He, K. Nitrate-driven urban haze pollution during summertime over the North China Plain. *Atmos. Chem. Phys.* **2018**, *18* (8), 5293−5306.

(3) Foret, G.; Michoud, V.; Kotthaus, S.; Petit, J. E.; Baudic, A.; Siour, G.; Kim, Y.; Doussin, J. F.; Dupont, J. C.; Formenti, P.; Gaimoz, C.; Ghersi, V.; Gratien, A.; Gros, V.; Jaffrezo, J. L.; Haeffelin, M.; Kreitz, M.; Ravetta, F.; Sartelet, K.; Simon, L.; Té, Y.; Uzu, G.; Zhang, S.; Favez, O.; Beekmann, M. The December 2016 extreme weather and particulate matter pollution episode in the Paris region (France). *Atmos. Environ.* **2022**, *291*, 119386.

(4) Franchin, A.; Fibiger, D. L.; Goldberger, L.; McDuffie, E. E.; Moravek, A.; Womack, C. C.; Crosman, E. T.; Docherty, K. S.; Dube, W. P.; Hoch, S. W.; Lee, B. H.; Long, R.; Murphy, J. G.; Thornton, J. A.; Brown, S. S.; Baasandorj, M.; Middlebrook, A. M. Airborne and ground-based observations of ammonium-nitrate-dominated aerosols in a shallow boundary layer during intense winter pollution episodes in northern Utah. *Atmos. Chem. Phys.* **2018**, *18* (23), 17259−17276.

(5) Zhang, Y.; Tian, J.; Wang, Q.; Qi, L.; Manousakas, M. I.; Han, Y.; Ran, W.; Sun, Y.; Liu, H.; Zhang, R.; Wu, Y.; Cui, T.; Daellenbach, K. R.; Slowik, J. G.; Prévôt, A. S. H.; Cao, J. High-time-resolution chemical composition and source apportionment of PM2.5 in northern Chinese cities: implications for policy. *Atmos. Chem. Phys.* **2023**, *23* (16), 9455−9471.

(6) Yu, W.; Xu, R.; Ye, T.; Abramson, M. J.; Morawska, L.; Jalaludin, B.; Johnston, F. H.; Henderson, S. B.; Knibbs, L. D.; Morgan, G. G.; Lavigne, E.; Heyworth, J.; Hales, S.; Marks, G. B.; Woodward, A.; Bell, M. L.; Samet, J. M.; Song, J.; Li, S.; Guo, Y. Estimates of global mortality burden associated with short-term exposure to fine particulate matter ($PM_{2.5}$). *Lancet Planet. Health* **2024**, *8* (3), e146−e155.

(7) Lu, X.; Mao, Q.; Gilliam, F. S.; Luo, Y.; Mo, J. Nitrogen deposition contributes to soil acidification in tropical ecosystems. *Glob Chang Biol.* **2014**, *20* (12), 3790−3801.

(8) Bouwman, A. F.; Van Vuuren, D. P.; Derwent, R. G.; Posch, M. A Global Analysis of Acidification and Eutrophication of Terrestrial Ecosystems. *Water, Air, Soil Pollut.* **2002**, *141* (1/4), 349−382.

(9) Clark, C. M.; Tilman, D. Loss of plant species after chronic low-level nitrogen deposition to prairie grasslands. *Nature* **2008**, *451* (7179), 712−715.

(10) Attwood, A. R.; Washenfelder, R. A.; Brock, C. A.; Hu, W.; Baumann, K.; Campuzano-Jost, P.; Day, D. A.; Edgerton, E. S.; Murphy, D. M.; Palm, B. B.; McComiskey, A.; Wagner, N. L.; de Sá, S. S.; Ortega, A.; Martin, S. T.; Jimenez, J. L.; Brown, S. S. Trends in sulfate and organic aerosol mass in the Southeast U.S.: Impact on

aerosol optical depth and radiative forcing. *Geophys. Res. Lett.* **2014**, *41* (21), 7701−7709.
(11) Zhai, S.; Jacob, D. J.; Wang, X.; Shen, L.; Li, K.; Zhang, Y.; Gui, K.; Zhao, T.; Liao, H. Fine particulate matter (PM2.5) trends in China, 2013−2018: separating contributions from anthropogenic emissions and meteorology. *Atmos. Chem. Phys.* **2019**, *19* (16), 11031−11041.
(12) Li, H.; Cheng, J.; Zhang, Q.; Zheng, B.; Zhang, Y.; Zheng, G.; He, K. Rapid transition in winter aerosol composition in Beijing from 2014 to 2017: response to clean air actions. *Atmos. Chem. Phys.* **2019**, *19* (17), 11485−11499.
(13) Shah, V.; Jaegle, L.; Thornton, J. A.; Lopez-Hilfiker, F. D.; Lee, B. H.; Schroder, J. C.; Campuzano-Jost, P.; Jimenez, J. L.; Guo, H. Y.; Sullivan, A. P.; Weber, R. J.; Green, J. R.; Fiddler, M. N.; Bililign, S.; Campos, T. L.; Stell, M.; Weinheimer, A. J.; Montzka, D. D.; Brown, S. S. Chemical feedbacks weaken the wintertime response of particulate sulfate and nitrate to emissions reductions over the eastern United States. *Proc. Natl. Acad. Sci. U.S.A.* **2018**, *115* (32), 8110−8115.
(14) Zhai, S.; Jacob, D. J.; Wang, X.; Liu, Z.; Wen, T.; Shah, V.; Li, K.; Moch, J. M.; Bates, K. H.; Song, S.; Shen, L.; Zhang, Y.; Luo, G.; Yu, F.; Sun, Y.; Wang, L.; Qi, M.; Tao, J.; Gui, K.; Xu, H.; Zhang, Q.; Zhao, T.; Wang, Y.; Lee, H. C.; Choi, H.; Liao, H. Control of particulate nitrate air pollution in China. *Nat. Geosci.* **2021**, *14* (6), 389−395.
(15) Chuang, M.-T.; Chou, C. C. K.; Hsiao, T.-C.; Lin, K.-y.; Lin, N.-H.; Lin, W.-Y.; Wang, S.-H.; Pani, S. K.; Lee, C.-T. Analyzing the increasing importance of nitrate in Taiwan from long-term trend of measurements. *Atmos. Environ.* **2021**, *267*, 118749.
(16) Fu, X.; Wang, T.; Gao, J.; Wang, P.; Liu, Y.; Wang, S.; Zhao, B.; Xue, L. Persistent Heavy Winter Nitrate Pollution Driven by Increased Photochemical Oxidants in Northern China. *Environ. Sci. Technol.* **2020**, *54* (7), 3881−3889.
(17) Song, S. J.; Nenes, A.; Gao, M.; Zhang, Y. Z.; Liu, P. F.; Shao, J. Y.; Ye, D. C.; Xu, W. Q.; Lei, L.; Sun, Y. L.; Liu, B. X.; Wang, S. X.; McElroy, M. B. Thermodynamic Modeling Suggests Declines in Water Uptake and Acidity of Inorganic Aerosols in Beijing Winter Haze Events during 2014/2015−2018/2019. *Environ. Sci. Technol. Lett.* **2019**, *6* (12), 752−760.
(18) Guo, H.; Otjes, R.; Schlag, P.; Kiendler-Scharr, A.; Nenes, A.; Weber, R. J. Effectiveness of ammonia reduction on control of fine particle nitrate. *Atmos. Chem. Phys.* **2018**, *18* (16), 12241−12256.
(19) Zhang, L.; Jacob, D. J.; Knipping, E. M.; Kumar, N.; Munger, J. W.; Carouge, C. C.; van Donkelaar, A.; Wang, Y. X.; Chen, D. Nitrogen deposition to the United States: distribution, sources, and processes. *Atmos. Chem. Phys.* **2012**, *12* (10), 4539−4554.
(20) Liu, L.; Xu, W.; Lu, X.; Zhong, B.; Guo, Y.; Lu, X.; Zhao, Y.; He, W.; Wang, S.; Zhang, X.; Liu, X.; Vitousek, P. Exploring global changes in agricultural ammonia emissions and their contribution to nitrogen deposition since 1980. *Proc. Natl. Acad. Sci. U.S.A.* **2022**, *119* (14), No. e2121998119.
(21) Van Damme, M.; Clarisse, L.; Whitburn, S.; Hadji-Lazaro, J.; Hurtmans, D.; Clerbaux, C.; Coheur, P.-F. Industrial and agricultural ammonia point sources exposed. *Nature* **2018**, *564* (7734), 99−103.
(22) Chen, Y.; Zhang, Q.; Cai, X.; Zhang, H.; Lin, H.; Zheng, C.; Guo, Z.; Hu, S.; Chen, L.; Tao, S.; Liu, M.; Wang, X. Rapid Increase in China's Industrial Ammonia Emissions: Evidence from Unit-Based Mapping. *Environ. Sci. Technol.* **2022**, *56* (6), 3375−3385.
(23) Farren, N. J.; Davison, J.; Rose, R. A.; Wagner, R. L.; Carslaw, D. C. Underestimated Ammonia Emissions from Road Vehicles. *Environ. Sci. Technol.* **2020**, *54* (24), 15689−15697.
(24) Shen, L.; Jacob, D. J.; Zhu, L.; Zhang, Q.; Zheng, B.; Sulprizio, M. P.; Li, K.; De Smedt, I.; González Abad, G.; Cao, H.; Fu, T.-M.; Liao, H. The 2005−2016 Trends of Formaldehyde Columns Over China Observed by Satellites: Increasing Anthropogenic Emissions of Volatile Organic Compounds and Decreasing Agricultural Fire Emissions. *Geophys. Res. Lett.* **2019**, *46* (8), 4468−4475.
(25) Nenes, A.; Pandis, S. N.; Weber, R. J.; Russell, A. Aerosol pH and liquid water content determine when particulate matter is sensitive to ammonia and nitrate availability. *Atmos. Chem. Phys.* **2020**, *20* (5), 3249−3258.
(26) Petetin, H.; Sciare, J.; Bressi, M.; Gros, V.; Rosso, A.; Sanchez, O.; Sarda-Estève, R.; Petit, J. E.; Beekmann, M. Assessing the ammonium nitrate formation regime in the Paris megacity and its representation in the CHIMERE model. *Atmos. Chem. Phys.* **2016**, *16* (16), 10419−10440.
(27) Xu, Z.; Liu, M.; Zhang, M.; Song, Y.; Wang, S.; Zhang, L.; Xu, T.; Wang, T.; Yan, C.; Zhou, T.; Sun, Y.; Pan, Y.; Hu, M.; Zheng, M.; Zhu, T. High efficiency of livestock ammonia emission controls in alleviating particulate nitrate during a severe winter haze episode in northern China. *Atmos. Chem. Phys.* **2019**, *19* (8), 5605−5613.
(28) Womack, C. C.; McDuffie, E. E.; Edwards, P. M.; Bares, R.; de Gouw, J. A.; Docherty, K. S.; Dubé, W. P.; Fibiger, D. L.; Franchin, A.; Gilman, J. B.; Goldberger, L.; Lee, B. H.; Lin, J. C.; Long, R.; Middlebrook, A. M.; Millet, D. B.; Moravek, A.; Murphy, J. G.; Quinn, P. K.; Riedel, T. P.; Roberts, J. M.; Thornton, J. A.; Valin, L. C.; Veres, P. R.; Whitehill, A. R.; Wild, R. J.; Warneke, C.; Yuan, B.; Baasandorj, M.; Brown, S. S. An Odd Oxygen Framework for Wintertime Ammonium Nitrate Aerosol Pollution in Urban Areas: NOx and VOC Control as Mitigation Strategies. *Geophys. Res. Lett.* **2019**, *46* (9), 4971−4979.
(29) Romer Present, P. S.; Zare, A.; Cohen, R. C. The changing role of organic nitrates in the removal and transport of NO_x. *Atmos. Chem. Phys.* **2020**, *20* (1), 267−279.
(30) Zhai, S.; Jacob, D. J.; Pendergrass, D. C.; Colombi, N. K.; Shah, V.; Yang, L. H.; Zhang, Q.; Wang, S.; Kim, H.; Sun, Y.; Choi, J. S.; Park, J. S.; Luo, G.; Yu, F.; Woo, J. H.; Kim, Y.; Dibb, J. E.; Lee, T.; Han, J. S.; Anderson, B. E.; Li, K.; Liao, H. Coarse particulate matter air quality in East Asia: implications for fine particulate nitrate. *Atmos. Chem. Phys.* **2023**, *23* (7), 4271−4281.
(31) Ansari, A. S.; Pandis, S. N. Response of Inorganic PM to Precursor Concentrations. *Environ. Sci. Technol.* **1998**, *32* (18), 2706−2714.
(32) Li, M.; Zhang, Z.; Yao, Q.; Wang, T.; Xie, M.; Li, S.; Zhuang, B.; Han, Y. Nonlinear responses of particulate nitrate to NO_x emission controls in the megalopolises of China. *Atmos. Chem. Phys.* **2021**, *21* (19), 15135−15152.
(33) Martin, R. V.; Chance, K.; Jacob, D. J.; Kurosu, T. P.; Spurr, R. J. D.; Bucsela, E.; Gleason, J. F.; Palmer, P. I.; Bey, I.; Fiore, A. M.; Li, Q.; Yantosca, R. M.; Koelemeijer, R. B. A. An improved retrieval of tropospheric nitrogen dioxide from GOME. *J. Geophys. Res. Atmos.* **2002**, *107* (D20), ACH 9−1−ACH 9−21.
(34) Lamsal, L. N.; Krotkov, N. A.; Vasilkov, A.; Marchenko, S.; Qin, W.; Yang, E. S.; Fasnacht, Z.; Joiner, J.; Choi, S.; Haffner, D.; Swartz, W. H.; Fisher, B.; Bucsela, E. Ozone Monitoring Instrument (OMI) Aura nitrogen dioxide standard product version 4.0 with improved surface and cloud treatments. *Atmos. Meas. Technol.* **2021**, *14* (1), 455−479.
(35) van Geffen, J.; Boersma, K. F.; Eskes, H.; Sneep, M.; ter Linden, M.; Zara, M.; Veefkind, J. P. S5P TROPOMI NO_2 slant column retrieval: method, stability, uncertainties and comparisons with OMI. *Atmos. Meas. Technol.* **2020**, *13* (3), 1315−1335.
(36) Kim, J.; Jeong, U.; Ahn, M.-H.; Kim, J. H.; Park, R. J.; Lee, H.; Song, C. H.; Choi, Y.-S.; Lee, K.-H.; Yoo, J.-M.; Jeong, M.-J.; Park, S. K.; Lee, K.-M.; Song, C.-K.; Kim, S.-W.; Kim, Y. J.; Kim, S.-W.; Kim, M.; Go, S.; Liu, X.; Chance, K.; Chan Miller, C.; Al-Saadi, J.; Veihelmann, B.; Bhartia, P. K.; Torres, O.; Abad, G. G.; Haffner, D. P.; Ko, D. H.; Lee, S. H.; Woo, J.-H.; Chong, H.; Park, S. S.; Nicks, D.; Choi, W. J.; Moon, K.-J.; Cho, A.; Yoon, J.; Kim, S.-k.; Hong, H.; Lee, K.; Lee, H.; Lee, S.; Choi, M.; Veefkind, P.; Levelt, P. F.; Edwards, D. P.; Kang, M.; Eo, M.; Bak, J.; Baek, K.; Kwon, H.-A.; Yang, J.; Park, J.; Han, K. M.; Kim, B.-R.; Shin, H.-W.; Choi, H.; Lee, E.; Chong, J.; Cha, Y.; Koo, J.-H.; Irie, H.; Hayashida, S.; Kasai, Y.; Kanaya, Y.; Liu, C.; Lin, J.; Crawford, J. H.; Carmichael, G. R.; Newchurch, M. J.; Lefer, B. L.; Herman, J. R.; Swap, R. J.; Lau, A. K. H.; Kurosu, T. P.; Jaross, G.; Ahlers, B.; Dobber, M.; McElroy, C. T.; Choi, Y. New Era of Air Quality Monitoring from Space:

Geostationary Environment Monitoring Spectrometer (GEMS). *Bull. Am. Meteorol. Soc.* **2020**, *101* (1), E1−E22.
(37) Zoogman, P.; Liu, X.; Suleiman, R. M.; Pennington, W. F.; Flittner, D. E.; Al-Saadi, J. A.; Hilton, B. B.; Nicks, D. K.; Newchurch, M. J.; Carr, J. L.; Janz, S. J.; Andraschko, M. R.; Arola, A.; Baker, B. D.; Canova, B. P.; Chan Miller, C.; Cohen, R. C.; Davis, J. E.; Dussault, M. E.; Edwards, D. P.; Fishman, J.; Ghulam, A.; González Abad, G.; Grutter, M.; Herman, J. R.; Houck, J.; Jacob, D. J.; Joiner, J.; Kerridge, B. J.; Kim, J.; Krotkov, N. A.; Lamsal, L.; Li, C.; Lindfors, A.; Martin, R. V.; McElroy, C. T.; McLinden, C.; Natraj, V.; Neil, D. O.; Nowlan, C. R.; O'Sullivan, E.; Palmer, P. I.; Pierce, R. B.; Pippin, M. R.; Saiz-Lopez, A.; Spurr, R. J. D.; Szykman, J. J.; Torres, O.; Veefkind, J. P.; Veihelmann, B.; Wang, H.; Wang, J.; Chance, K. Tropospheric emissions: Monitoring of pollution (TEMPO). *J. Quant. Spectrosc. Radiat. Transf.* **2017**, *186*, 17−39.
(38) Gulde, S.; Kolm, M.; Smith, D.; Maurer, R.; Bazalgette Courrèges-Lacoste, G.; Sallusti, M.; Bagnasco, G. *Sentinel 4: A Geostationary Imaging UVN Spectrometer for Air Quality Monitoring: Status of Design, Performance and Development*; SPIE, 2017.
(39) Beer, R.; Shephard, M. W.; Kulawik, S. S.; Clough, S. A.; Eldering, A.; Bowman, K. W.; Sander, S. P.; Fisher, B. M.; Payne, V. H.; Luo, M.; Osterman, G. B.; Worden, J. R. First satellite observations of lower tropospheric ammonia and methanol. *Geophys. Res. Lett.* **2008**, *35* (9), L09801.
(40) Clarisse, L.; Clerbaux, C.; Dentener, F.; Hurtmans, D.; Coheur, P.-F. Global ammonia distribution derived from infrared satellite observations. *Nat. Geosci.* **2009**, *2* (7), 479−483.
(41) Shephard, M. W.; Cady-Pereira, K. E. Cross-track Infrared Sounder (CrIS) satellite observations of tropospheric ammonia. *Atmos. Meas. Technol.* **2015**, *8* (3), 1323−1336.
(42) Lamarre, D.; Aminou, D.; van den Braembussche, P.; Hallibert, P.; Ahlers, B.; Wilson, M.; Luhmann, H. J. Meteosat Third Generation: The Infrared Sounder Instrument. *Imaging and Applied Optics*; Optica Publishing Group: Toronto, 2011; p JMA2. 2011/07/10.
(43) Dang, R.; Jacob, D. J.; Zhai, S.; Coheur, P.; Clarisse, L.; Van Damme, M.; Pendergrass, D. C.; Choi, J.-s.; Park, J.-s.; Liu, Z.; Liao, H. Diagnosing the Sensitivity of Particulate Nitrate to Precursor Emissions Using Satellite Observations of Ammonia and Nitrogen Dioxide. *Geophys. Res. Lett.* **2023**, *50* (24), No. e2023GL105761.
(44) Jin, X.; Fiore, A. M.; Murray, L. T.; Valin, L. C.; Lamsal, L. N.; Duncan, B.; Folkert Boersma, K.; De Smedt, I.; Abad, G. G.; Chance, K.; Tonnesen, G. S. Evaluating a Space-Based Indicator of Surface Ozone-NO_x-VOC Sensitivity Over Midlatitude Source Regions and Application to Decadal Trends. *J. Geophys. Res. Atmos.* **2017**, *122* (19), 10439−410461.
(45) Martin, R. V.; Fiore, A. M.; Van Donkelaar, A. Space-based diagnosis of surface ozone sensitivity to anthropogenic emissions. *Geophys. Res. Lett.* **2004**, *31* (6), L06120.
(46) Duncan, B. N.; Yoshida, Y.; Olson, J. R.; Sillman, S.; Martin, R. V.; Lamsal, L.; Hu, Y.; Pickering, K. E.; Retscher, C.; Allen, D. J.; Crawford, J. H. Application of OMI observations to a space-based indicator of NOx and VOC controls on surface ozone formation. *Atmos. Environ.* **2010**, *44* (18), 2213−2223.
(47) Zhu, L.; Jacob, D. J.; Mickley, L. J.; Marais, E. A.; Cohan, D. S.; Yoshida, Y.; Duncan, B. N.; González Abad, G.; Chance, K. V. Anthropogenic emissions of highly reactive volatile organic compounds in eastern Texas inferred from oversampling of satellite (OMI) measurements of HCHO columns. *Environ. Res. Lett.* **2014**, *9* (11), 114004.
(48) Wang, X.; Jacob, D. J.; Downs, W.; Zhai, S.; Zhu, L.; Shah, V.; Holmes, C. D.; Sherwen, T.; Alexander, B.; Evans, M. J.; Eastham, S. D.; Neuman, J. A.; Veres, P. R.; Koenig, T. K.; Volkamer, R.; Huey, L. G.; Bannan, T. J.; Percival, C. J.; Lee, B. H.; Thornton, J. A. Global tropospheric halogen (Cl, Br, I) chemistry and its impact on oxidants. *Atmos. Chem. Phys.* **2021**, *21* (18), 13973−13996.
(49) Fountoukis, C.; Nenes, A. ISORROPIA II: a computationally efficient thermodynamic equilibrium model for K+-Ca2+-Mg2+-Nh(4)(+)-Na+-SO42−NO3−Cl−H2O aerosols. *Atmos. Chem. Phys.* **2007**, *7* (17), 4639−4659.
(50) Fisher, J. A.; Jacob, D. J.; Travis, K. R.; Kim, P. S.; Marais, E. A.; Chan Miller, C.; Yu, K.; Zhu, L.; Yantosca, R. M.; Sulprizio, M. P.; Mao, J.; Wennberg, P. O.; Crounse, J. D.; Teng, A. P.; Nguyen, T. B.; St. Clair, J. M.; Cohen, R. C.; Romer, P.; Nault, B. A.; Wooldridge, P. J.; Jimenez, J. L.; Campuzano-Jost, P.; Day, D. A.; Hu, W.; Shepson, P. B.; Xiong, F.; Blake, D. R.; Goldstein, A. H.; Misztal, P. K.; Hanisco, T. F.; Wolfe, G. M.; Ryerson, T. B.; Wisthaler, A.; Mikoviny, T. Organic nitrate chemistry and its implications for nitrogen budgets in an isoprene- and monoterpene-rich atmosphere: constraints from aircraft (SEAC4RS) and ground-based (SOAS) observations in the Southeast US. *Atmos. Chem. Phys.* **2016**, *16* (9), 5969−5991.
(51) Alexander, B.; Park, R. J.; Jacob, D. J.; Li, Q. B.; Yantosca, R. M.; Savarino, J.; Lee, C. C. W.; Thiemens, M. H. Sulfate formation in sea-salt aerosols: Constraints from oxygen isotopes. *J. Geophys. Res. Atmos.* **2005**, *110*, D10307.
(52) Fairlie, T. D.; Jacob, D. J.; Dibb, J. E.; Alexander, B.; Avery, M. A.; van Donkelaar, A.; Zhang, L. Impact of mineral dust on nitrate, sulfate, and ozone in transpacific Asian pollution plumes. *Atmos. Chem. Phys.* **2010**, *10* (8), 3999−4012.
(53) Heald, C. L.; Collett, J. L., Jr; Lee, T.; Benedict, K. B.; Schwandner, F. M.; Li, Y.; Clarisse, L.; Hurtmans, D. R.; Van Damme, M.; Clerbaux, C.; Coheur, P. F.; Philip, S.; Martin, R. V.; Pye, H. O. T. Atmospheric ammonia and particulate inorganic nitrogen over the United States. *Atmos. Chem. Phys.* **2012**, *12* (21), 10295−10312.
(54) Bian, H.; Chin, M.; Hauglustaine, D. A.; Schulz, M.; Myhre, G.; Bauer, S. E.; Lund, M. T.; Karydis, V. A.; Kucsera, T. L.; Pan, X.; Pozzer, A.; Skeie, R. B.; Steenrod, S. D.; Sudo, K.; Tsigaridis, K.; Tsimpidi, A. P.; Tsyro, S. G. Investigation of global particulate nitrate from the AeroCom phase III experiment. *Atmos. Chem. Phys.* **2017**, *17* (21), 12911−12940.
(55) Luo, G.; Yu, F.; Schwab, J. Revised treatment of wet scavenging processes dramatically improves GEOS-Chem 12.0.0 simulations of surface nitric acid, nitrate, and ammonium over the United States. *Geosci. Model Dev.* **2019**, *12* (8), 3439−3447.
(56) Luo, G.; Yu, F.; Moch, J. M. Further improvement of wet process treatments in GEOS-Chem v12.6.0: impact on global distributions of aerosols and aerosol precursors. *Geosci. Model Dev.* **2020**, *13* (6), 2879−2903.
(57) Dang, R.; Jacob, D. J.; Shah, V.; Eastham, S. D.; Fritz, T. M.; Mickley, L. J.; Liu, T.; Wang, Y.; Wang, J. Background nitrogen dioxide (NO2) over the United States and its implications for satellite observations and trends: effects of nitrate photolysis, aircraft, and open fires. *Atmos. Chem. Phys.* **2023**, *23* (11), 6271−6284.
(58) McDuffie, E. E.; Smith, S. J.; O'Rourke, P.; Tibrewal, K.; Venkataraman, C.; Marais, E. A.; Zheng, B.; Crippa, M.; Brauer, M.; Martin, R. V. A global anthropogenic emission inventory of atmospheric pollutants from sector- and fuel-specific sources (1970−2017): an application of the Community Emissions Data System (CEDS). *Earth Syst. Sci. Data* **2020**, *12* (4), 3413−3442.
(59) Zheng, B.; Tong, D.; Li, M.; Liu, F.; Hong, C.; Geng, G.; Li, H.; Li, X.; Peng, L.; Qi, J.; Yan, L.; Zhang, Y.; Zhao, H.; Zheng, Y.; He, K.; Zhang, Q. Trends in China's anthropogenic emissions since 2010 as the consequence of clean air actions. *Atmos. Chem. Phys. Discuss.* **2018**, *2018*, 1−27.
(60) Woo, J.-H.; Kim, Y.; Kim, H.-K.; Choi, K.-C.; Eum, J.-H.; Lee, J.-B.; Lim, J.-H.; Kim, J.; Seong, M. Development of the CREATE Inventory in Support of Integrated Climate and Air Quality Modeling for Asia. *Sustainability* **2020**, *12* (19), 7930.
(61) van der Werf, G. R.; Randerson, J. T.; Giglio, L.; van Leeuwen, T. T.; Chen, Y.; Rogers, B. M.; Mu, M.; van Marle, M. J. E.; Morton, D. C.; Collatz, G. J.; Yokelson, R. J.; Kasibhatla, P. S. Global fire emissions estimates during 1997−2016. *Earth Syst. Sci. Data* **2017**, *9* (2), 697−720.
(62) Hudman, R. C.; Moore, N. E.; Mebust, A. K.; Martin, R. V.; Russell, A. R.; Valin, L. C.; Cohen, R. C. Steps towards a mechanistic model of global soil nitric oxide emissions: implementation and space based-constraints. *Atmos. Chem. Phys.* **2012**, *12* (16), 7779−7795.

(63) Wang, Y.; Ge, C.; Castro Garcia, L.; Jenerette, G. D.; Oikawa, P. Y.; Wang, J. Improved modelling of soil NOx emissions in a high temperature agricultural region: role of background emissions on NO2 trend over the US. *Environ. Res. Lett.* **2021**, *16* (8), 084061.
(64) Murray, L. T.; Jacob, D. J.; Logan, J. A.; Hudman, R. C.; Koshak, W. J. Optimized regional and interannual variability of lightning in a global chemical transport model constrained by LIS/OTD satellite data. *J. Geophys. Res. Atmos.* **2012**, *117*, D20307.
(65) Guenther, A. B.; Jiang, X.; Heald, C. L.; Sakulyanontvittaya, T.; Duhl, T.; Emmons, L. K.; Wang, X. The Model of Emissions of Gases and Aerosols from Nature version 2.1 (MEGAN2.1): an extended and updated framework for modeling biogenic emissions. *Geosci. Model Dev.* **2012**, *5* (6), 1471−1492.
(66) Huang, X.; Liu, Z.; Liu, J.; Hu, B.; Wen, T.; Tang, G.; Zhang, J.; Wu, F.; Ji, D.; Wang, L.; Wang, Y. Chemical characterization and source identification of PM2.5 at multiple sites in the Beijing−Tianjin−Hebei region, China. *Atmos. Chem. Phys.* **2017**, *17* (21), 12941−12962.
(67) Liu, Z.; Gao, W.; Yu, Y.; Hu, B.; Xin, J.; Sun, Y.; Wang, L.; Wang, G.; Bi, X.; Zhang, G.; Xu, H.; Cong, Z.; He, J.; Xu, J.; Wang, Y. Characteristics of $PM_{2.5}$ mass concentrations and chemical species in urban and background areas of China: emerging results from the CARE-China network. *Atmos. Chem. Phys.* **2018**, *18* (12), 8849−8871.
(68) Tan, T.; Hu, M.; Li, M.; Guo, Q.; Wu, Y.; Fang, X.; Gu, F.; Wang, Y.; Wu, Z. New insight into PM2.5 pollution patterns in Beijing based on one-year measurement of chemical compositions. *Sci. Total Environ.* **2018**, *621*, 734−743.
(69) Zhang, Q.; Zheng, Y.; Tong, D.; Shao, M.; Wang, S.; Zhang, Y.; Xu, X.; Wang, J.; He, H.; Liu, W.; Ding, Y.; Lei, Y.; Li, J.; Wang, Z.; Zhang, X.; Wang, Y.; Cheng, J.; Liu, Y.; Shi, Q.; Yan, L.; Geng, G.; Hong, C.; Li, M.; Liu, F.; Zheng, B.; Cao, J.; Ding, A.; Gao, J.; Fu, Q.; Huo, J.; Liu, B.; Liu, Z.; Yang, F.; He, K.; Hao, J. Drivers of improved $PM_{2.5}$ air quality in China from 2013 to 2017. *Proc. Natl. Acad. Sci. U.S.A.* **2019**, *116* (49), 24463−24469.
(70) Zhao, L.; Wang, L.; Tan, J.; Duan, J.; Ma, X.; Zhang, C.; Ji, S.; Qi, M.; Lu, X.; Wang, Y.; Wang, Q.; Xu, R. Changes of chemical composition and source apportionment of PM2.5 during 2013−2017 in urban Handan, China. *Atmos. Environ.* **2019**, *206*, 119−131.
(71) Kong, L.; Feng, M.; Liu, Y.; Zhang, Y.; Zhang, C.; Li, C.; Qu, Y.; An, J.; Liu, X.; Tan, Q.; Cheng, N.; Deng, Y.; Zhai, R.; Wang, Z. Elucidating the pollution characteristics of nitrate, sulfate and ammonium in $PM_{2.5}$ in Chengdu, southwest China, based on 3-year measurements. *Atmos. Chem. Phys.* **2020**, *20* (19), 11181−11199.
(72) Chow, W. S.; Liao, K.; Huang, X. H. H.; Leung, K. F.; Lau, A. K. H.; Yu, J. Z. Measurement report: The 10-year trend of PM2.5 major components and source tracers from 2008 to 2017 in an urban site of Hong Kong, China. *Atmos. Chem. Phys.* **2022**, *22* (17), 11557−11577.
(73) Sun, J.; Qin, M.; Xie, X.; Fu, W.; Qin, Y.; Sheng, L.; Li, L.; Li, J.; Sulaymon, I. D.; Jiang, L.; Huang, L.; Yu, X.; Hu, J. Seasonal modeling analysis of nitrate formation pathways in Yangtze River Delta region, China. *Atmos. Chem. Phys.* **2022**, *22* (18), 12629−12646.
(74) Xie, M.; Lu, X.; Ding, F.; Cui, W.; Zhang, Y.; Feng, W. Evaluating the influence of constant source profile presumption on PMF analysis of PM2.5 by comparing long- and short-term hourly observation-based modeling. *Environ. Pollut.* **2022**, *314*, 120273.
(75) Zang, H.; Zhao, Y.; Huo, J.; Zhao, Q.; Fu, Q.; Duan, Y.; Shao, J.; Huang, C.; An, J.; Xue, L.; Li, Z.; Li, C.; Xiao, H. High atmospheric oxidation capacity drives wintertime nitrate pollution in the eastern Yangtze River Delta of China. *Atmos. Chem. Phys.* **2022**, *22* (7), 4355−4374.
(76) Schiferl, L. D.; Heald, C. L.; Nowak, J. B.; Holloway, J. S.; Neuman, J. A.; Bahreini, R.; Pollack, I. B.; Ryerson, T. B.; Wiedinmyer, C.; Murphy, J. G. An investigation of ammonia and inorganic particulate matter in California during the CalNex campaign. *J. Geophys. Res. Atmos.* **2014**, *119* (4), 1883−1902.
(77) Van Damme, M.; Clarisse, L.; Franco, B.; Sutton, M. A.; Erisman, J. W.; Wichink Kruit, R.; van Zanten, M.; Whitburn, S.; Hadji-Lazaro, J.; Hurtmans, D.; Clerbaux, C.; Coheur, P.-F. Global, regional and national trends of atmospheric ammonia derived from a decadal (2008−2018) satellite record. *Environ. Res. Lett.* **2021**, *16* (5), 055017.
(78) Clarisse, L.; Franco, B.; Van Damme, M.; Di Gioacchino, T.; Hadji-Lazaro, J.; Whitburn, S.; Noppen, L.; Hurtmans, D.; Clerbaux, C.; Coheur, P. The IASI NH3 version 4 product: averaging kernels and improved consistency. *Atmos. Meas. Technol.* **2023**, *16* (21), 5009−5028.
(79) Van Damme, M.; Clarisse, L.; Heald, C. L.; Hurtmans, D.; Ngadi, Y.; Clerbaux, C.; Dolman, A. J.; Erisman, J. W.; Coheur, P. F. Global distributions, time series and error characterization of atmospheric ammonia (NH_3) from IASI satellite observations. *Atmos. Chem. Phys.* **2014**, *14* (6), 2905−2922.
(80) Paulot, F.; Jacob, D. J.; Pinder, R. W.; Bash, J. O.; Travis, K.; Henze, D. K. Ammonia emissions in the United States, European Union, and China derived by high-resolution inversion of ammonium wet deposition data: Interpretation with a new agricultural emissions inventory (MASAGE_NH3). *J. Geophys. Res. Atmos.* **2014**, *119* (7), 4343−4364.
(81) Cooper, M. J.; Martin, R. V.; Henze, D. K.; Jones, D. B. A. Effects of a priori profile shape assumptions on comparisons between satellite NO2 columns and model simulations. *Atmos. Chem. Phys.* **2020**, *20* (12), 7231−7241.
(82) Whitburn, S.; Van Damme, M.; Clarisse, L.; Bauduin, S.; Heald, C. L.; Hadji-Lazaro, J.; Hurtmans, D.; Zondlo, M. A.; Clerbaux, C.; Coheur, P.-F. A flexible and robust neural network IASI-NH3 retrieval algorithm. *J. Geophys. Res. Atmos.* **2016**, *121* (11), 6581−6599.
(83) Shah, V.; Jacob, D. J.; Dang, R.; Lamsal, L. N.; Strode, S. A.; Steenrod, S. D.; Boersma, K. F.; Eastham, S. D.; Fritz, T. M.; Thompson, C.; Peischl, J.; Bourgeois, I.; Pollack, I. B.; Nault, B. A.; Cohen, R. C.; Campuzano-Jost, P.; Jimenez, J. L.; Andersen, S. T.; Carpenter, L. J.; Sherwen, T.; Evans, M. J. Nitrogen oxides in the free troposphere: implications for tropospheric oxidants and the interpretation of satellite NO2 measurements. *Atmos. Chem. Phys.* **2023**, *23* (2), 1227−1257.
(84) Silvern, R. F.; Jacob, D. J.; Mickley, L. J.; Sulprizio, M. P.; Travis, K. R.; Marais, E. A.; Cohen, R. C.; Laughner, J. L.; Choi, S.; Joiner, J.; Lamsal, L. N. Using satellite observations of tropospheric NO_2 columns to infer long-term trends in US NO_x emissions: the importance of accounting for the free tropospheric NO_2 background. *Atmos. Chem. Phys.* **2019**, *19* (13), 8863−8878.
(85) Luo, Z.; Zhang, Y.; Chen, W.; Van Damme, M.; Coheur, P. F.; Clarisse, L. Estimating global ammonia (NH3) emissions based on IASI observations from 2008 to 2018. *Atmos. Chem. Phys.* **2022**, *22* (15), 10375−10388.
(86) Ren, C.; Huang, X.; Wang, Z.; Sun, P.; Chi, X.; Ma, Y.; Zhou, D.; Huang, J.; Xie, Y.; Gao, J.; Ding, A. Nonlinear response of nitrate to NOx reduction in China during the COVID-19 pandemic. *Atmos. Environ.* **2021**, *264*, 118715.
(87) Balamurugan, V.; Chen, J.; Qu, Z.; Bi, X.; Keutsch, F. N. Secondary PM2.5 decreases significantly less than NO2 emission reductions during COVID lockdown in Germany. *Atmos. Chem. Phys.* **2022**, *22* (11), 7105−7129.
(88) Yang, S.; Yuan, B.; Peng, Y.; Huang, S.; Chen, W.; Hu, W.; Pei, C.; Zhou, J.; Parrish, D. D.; Wang, W.; He, X.; Cheng, C.; Li, X. B.; Yang, X.; Song, Y.; Wang, H.; Qi, J.; Wang, B.; Wang, C.; Wang, C.; Wang, Z.; Li, T.; Zheng, E.; Wang, S.; Wu, C.; Cai, M.; Ye, C.; Song, W.; Cheng, P.; Chen, D.; Wang, X.; Zhang, Z.; Wang, X.; Zheng, J.; Shao, M. The formation and mitigation of nitrate pollution: comparison between urban and suburban environments. *Atmos. Chem. Phys.* **2022**, *22* (7), 4539−4556.
(89) Wen, L.; Xue, L.; Wang, X.; Xu, C.; Chen, T.; Yang, L.; Wang, T.; Zhang, Q.; Wang, W. Summertime fine particulate nitrate pollution in the North China Plain: increasing trends, formation mechanisms and implications for control policy. *Atmos. Chem. Phys.* **2018**, *18* (15), 11261−11275.

(90) Zheng, M.; Wang, Y.; Bao, J.; Yuan, L.; Zheng, H.; Yan, Y.; Liu, D.; Xie, M.; Kong, S. Initial Cost Barrier of Ammonia Control in Central China. *Geophys. Res. Lett.* **2019**, *46* (23), 14175−14184.
(91) Paglione, M.; Decesari, S.; Rinaldi, M.; Tarozzi, L.; Manarini, F.; Gilardoni, S.; Facchini, M. C.; Fuzzi, S.; Bacco, D.; Trentini, A.; Pandis, S. N.; Nenes, A. Historical Changes in Seasonal Aerosol Acidity in the Po Valley (Italy) as Inferred from Fog Water and Aerosol Measurements. *Environ. Sci. Technol.* **2021**, *55* (11), 7307−7315.
(92) Petit, J. E.; Dupont, J. C.; Favez, O.; Gros, V.; Zhang, Y.; Sciare, J.; Simon, L.; Truong, F.; Bonnaire, N.; Amodeo, T.; Vautard, R.; Haeffelin, M. Response of atmospheric composition to COVID-19 lockdown measures during spring in the Paris region (France). *Atmos. Chem. Phys.* **2021**, *21* (22), 17167−17183.
(93) Pusede, S. E.; Duffey, K. C.; Shusterman, A. A.; Saleh, A.; Laughner, J. L.; Wooldridge, P. J.; Zhang, Q.; Parworth, C. L.; Kim, H.; Capps, S. L.; Valin, L. C.; Cappa, C. D.; Fried, A.; Walega, J.; Nowak, J. B.; Weinheimer, A. J.; Hoff, R. M.; Berkoff, T. A.; Beyersdorf, A. J.; Olson, J.; Crawford, J. H.; Cohen, R. C. On the effectiveness of nitrogen oxide reductions as a control over ammonium nitrate aerosol. *Atmos. Chem. Phys.* **2016**, *16* (4), 2575−2596.
(94) Kelly, J. T.; Parworth, C. L.; Zhang, Q.; Miller, D. J.; Sun, K.; Zondlo, M. A.; Baker, K. R.; Wisthaler, A.; Nowak, J. B.; Pusede, S. E.; Cohen, R. C.; Weinheimer, A. J.; Beyersdorf, A. J.; Tonnesen, G. S.; Bash, J. O.; Valin, L. C.; Crawford, J. H.; Fried, A.; Walega, J. G. Modeling NH4NO3 Over the San Joaquin Valley During the 2013 DISCOVER-AQ Campaign. *J. Geophys. Res. Atmos.* **2018**, *123* (9), 4727−4745.
(95) Prabhakar, G.; Parworth, C. L.; Zhang, X.; Kim, H.; Young, D. E.; Beyersdorf, A. J.; Ziemba, L. D.; Nowak, J. B.; Bertram, T. H.; Faloona, I. C.; Zhang, Q.; Cappa, C. D. Observational assessment of the role of nocturnal residual-layer chemistry in determining daytime surface particulate nitrate concentrations. *Atmos. Chem. Phys.* **2017**, *17* (23), 14747−14770.
(96) Zhai, T.; Lu, K.; Wang, H.; Lou, S.; Chen, X.; Hu, R.; Zhang, Y. Elucidate the formation mechanism of particulate nitrate based on direct radical observations in the Yangtze River Delta summer 2019. *Atmos. Chem. Phys.* **2023**, *23* (4), 2379−2391.
(97) Tan, Z.; Wang, H.; Lu, K.; Dong, H.; Liu, Y.; Zeng, L.; Hu, M.; Zhang, Y. An Observational Based Modeling of the Surface Layer Particulate Nitrate in the North China Plain During Summertime. *J. Geophys. Res. Atmos.* **2021**, *126* (18), No. e2021JD035623.
(98) Yang, Y.; Zhao, Y.; Zhang, L.; Zhang, J.; Huang, X.; Zhao, X.; Zhang, Y.; Xi, M.; Lu, Y. Improvement of the satellite-derived NO_x emissions on air quality modeling and its effect on ozone and secondary inorganic aerosol formation in the Yangtze River Delta, China. *Atmos. Chem. Phys.* **2021**, *21* (2), 1191−1209.
(99) Lin, Y. C.; Zhang, Y. L.; Fan, M. Y.; Bao, M. Heterogeneous formation of particulate nitrate under ammonium-rich regimes during the high-$PM_{2.5}$ events in Nanjing, China. *Atmos. Chem. Phys.* **2020**, *20* (6), 3999−4011.
(100) Lambert, J.-C.; Keppens, A.; Compernolle, S.; Eichmann, K.-U.; de Graaf, M.; Hubert, D.; Langerock, B.; Ludewig, A.; Sha, M. K.; Verhoelst, T.; Wagner, T.; Ahn, C.; Argyrouli, A.; Balis, D.; Chan, K. L.; Coldewey-Egbers, M.; De Smedt, I.; Eskes, H.; Fjæraa, A. M.; Garane, K.; Gleason, J. F.; Goutail, F.; Granville, J.; Hedelt, P.; Ahn, C.; Heue, K.-P.; Jaross, G.; Kleipool, Q.; Koukouli, M.; Lutz, R.; Martinez Velarte, M. C.; Michailidis, K.; Nanda, S.; Niemeijer, S.; Pazmiño, A.; Pinardi, G.; Richter, A.; Rozemeijer, N.; Sneep, M.; Stein Zweers, D.; Theys, N.; Tilstra, G.; Torres, O.; Valks, P.; van Geffen, J.; Vigouroux, C.; Wang, P.; Weber, M. *Quarterly Validation Report of the Copernicus Sentinel-5 Precursor Operational Data Products #23: April 2018−May 2024*, 2024. https://s5p-mpc-vdaf.aeronomie.be/ProjectDir/reports//pdf/S5P-MPC-IASB-ROCVR-23.00.00_FINAL_signed.pdf.
(101) Oak, Y. J.; Jacob, D. J.; Balasus, N.; Yang, L. H.; Chong, H.; Park, J.; Lee, H.; Lee, G. T.; Ha, E. S.; Park, R. J.; Kwon, H. A.; Kim, J. A bias-corrected GEMS geostationary satellite product for nitrogen dioxide using machine learning to enforce consistency with the TROPOMI satellite instrument. *EGUsphere* **2024**, *2024*, 1−19.
(102) Marais, E. A.; Pandey, A. K.; Van Damme, M.; Clarisse, L.; Coheur, P.-F.; Shephard, M. W.; Cady-Pereira, K. E.; Misselbrook, T.; Zhu, L.; Luo, G.; Yu, F. UK Ammonia Emissions Estimated With Satellite Observations and GEOS-Chem. *J. Geophys. Res. Atmos.* **2021**, *126* (18), No. e2021JD035237.
(103) Cady-Pereira, K. E.; Guo, X.; Wang, R.; Leytem, A. B.; Calkins, C.; Berry, E.; Sun, K.; Müller, M.; Wisthaler, A.; Payne, V. H.; Shephard, M. W.; Zondlo, M. A.; Kantchev, V. Validation of MUSES NH3 observations from AIRS and CrIS against aircraft measurements from DISCOVER-AQ and a surface network in the Magic Valley. *Atmos. Meas. Technol.* **2024**, *17* (1), 15−36.
(104) Schmit, T. J.; Li, Z.; Gunshor, M. M.; Iturbide-Iturbide, F.; Yoe, J. G.; McCorkel, J.; Heidinger, A. U.S. Plans for Geostationary Hyperspectral Infrared Sounders. *IGARSS 2022—2022 IEEE International Geoscience and Remote Sensing Symposium*, 2022; pp 5411−5414. 17−22 July 2022.
(105) Coheur, P.-F.; Levelt, P.; Clarisse, L.; van Damme, M.; Eskes, H.; Veefkind, J. P.; Clerbaux, C.; Dentener, F. J.; Erisman, J. W.; Schaap, M.; Sutton, M. A.; Van Roozendael, M. Nitrosat, a satellite mission concept for mapping reactive nitrogen at the landscape scale. *EGU General Assembly 2021, Online*, 2021.

https://doi.org/10.1021/acs.est.4c08082
Environ. Sci. Technol. 2024, 58, 20101−20113